

# Frequency-specific modeling for battery parameter identification under battery aging

Ying Kung, Cheng Hsi Tien, Chi-Jyun Ko, Kuo-Ching Chen\*

*Institute of Applied Mechanics, National Taiwan University, 1, Sec. 4, Roosevelt Rd., Taipei 10617,  
Taiwan*

\* Corresponding author.

E-mail address: [kcc@iam.ntu.edu.tw](mailto:kcc@iam.ntu.edu.tw) (K.C. Chen).

## ABSTRACT

We present a segment-specific, physics-informed machine learning framework for rapid, accurate, and interpretable estimation of key electrochemical parameters from partial Electrochemical Impedance Spectrum (EIS) measurements. Experimental EIS data were collected on commercial LGM50T cells over 95 %–60 % SOH. A GA-calibrated P2D model was used solely to generate high-fidelity nominal parameters (error  $\approx 1.95\%$ ) for training labels. To reduce the cost of full-spectrum inversion, we apply a two-stage Sobol sensitivity filtering in arbitrary segment order: first on any chosen frequency band (low, mid, or high) to select its three most influential parameters, then on a second band to select three more from the remainder. Each band-specific Transformer, trained on 20,000 samples varying only its three segment-sensitive parameters, predicts its targets in under 0.3 s and reconstructs the corresponding impedance arc with MAPE < 1 % (for SOH  $\geq 75\%$ ) or < 3 % even under severe aging. The models recover known aging trends—e.g. solid-phase diffusion decay and film-resistance growth—validating physical consistency. Compared to full-spectrum GA inversion, our approach reduces computation by five orders of magnitude while preserving fidelity and interpretability. This work demonstrates that any single frequency segment alone suffices for real-time, onboard BMS parameter identification.

*Keywords:* Lithium-ion batteries · EIS · Parameter identification · P2D modeling · Transformer · Sobol sensitivity · Battery aging

## 1. Introduction

As lithium-ion batteries (LIBs) continue to dominate the energy storage landscape—from electric vehicles (EVs) to grid-scale backup systems—the demand for rapid, reliable, and interpretable diagnostic tools becomes increasingly critical. Catastrophic failures linked to undetected degradation, as well as the rise of real-time battery health management in modern battery management systems (BMS), underscore the need for actionable, fast diagnostics rooted in physical insight.

EIS has emerged as a non-destructive, high-resolution technique that probes a battery's dynamic response across a wide frequency range, providing insights into charge transfer resistance, ion diffusion, and SEI formation [1,2]. Because EIS reflects a wide range of electrochemical dynamics across multiple time scales, it has been widely used for health estimation, aging analysis, and degradation mode diagnosis [3]. However, translating EIS data into meaningful electrochemical parameters remains challenging due to the inherent ambiguity in parameter identification from EIS data [4]. Conventional approaches such as equivalent circuit modeling (ECM) or black-box optimization methods often require extensive tuning, suffer from low generalizability, and are limited in interpretability [5,6].

Although various techniques have been developed for electrochemical parameter identification, several critical limitations persist. The inverse problem is inherently underdetermined—multiple parameter sets can yield similar impedance or voltage responses, making unique identification challenging. In addition, many frameworks rely on full voltage–current time series as input, which is impractical for online diagnostics or embedded battery management systems. Optimization-based methods such as genetic algorithms (GA) or particle swarm optimization (PSO) are computationally expensive, often requiring hours or days of offline processing. Lastly, while some deep learning models

achieve high predictive accuracy, they often lack physical interpretability, making it difficult to link predicted parameters to real degradation mechanisms.

To address these challenges, researchers have increasingly turned to physics-based electrochemical models such as the Doyle–Fuller–Newman (DFN) or pseudo-two-dimensional (P2D) model, which offer mechanistic insight and directly link model parameters to underlying physical processes [7]. Simultaneously, machine learning (ML) techniques have gained traction for parameter estimation, surrogate modeling, and health prediction due to their flexibility and computational efficiency [8,9]. Recent studies have revealed that not all electrochemical parameters equally influence the impedance spectrum—only a subset dominates within specific frequency regions, enabling more efficient model simplification [10]. Furthermore, impedance responses in different frequency bands have been consistently linked to distinct physical mechanisms: low frequencies reflect mass transport effects, mid frequencies are dominated by charge transfer resistance, and high frequencies correspond primarily to ohmic processes [11]. This segmentation not only enhances interpretability, but also provides a physically grounded basis for targeted parameter estimation. In addition, recent work comparing equivalent circuit models under varying operating conditions demonstrated that impedance components associated with specific frequency bands (e.g., Warburg-related mass transfer resistance and cathodic activation losses) respond monotonically to external factors such as humidity and pressure—further validating the connection between frequency-domain behavior and internal physical processes [12].

In response, several frameworks have been proposed. Some estimate parameters from partial voltage or  $dQ/dV$  data [13], simplifying input requirements but forgoing frequency-domain detail. Other approaches retain full P2D models, combining them with GA or 1D-CNNs to predict aging-related parameters [14], though they often require full voltage–current profiles and exhibit slow convergence. Reduced-order models like ROESPM [15] and SPME [16] improve speed at the cost of reduced physical resolution. Additionally, PSO-based optimization under extreme aging scenarios (e.g.,

overcharge/discharge) has shown robustness in extracting solid-phase diffusion and reaction parameters [17], though it still requires full voltage inputs and suffers from long computation times. Fractional-order and hybrid GA–PSO methods [18] extend fitting capabilities but remain unsuitable for real-time applications due to their long computation cycles.

Recently, neural network–based pipelines such as GANCO, DNN–Fisher [19], and GA–DNN [20] have achieved promising accuracy in predicting large parameter sets. However, they typically demand massive datasets, extensive training times (e.g., multiple weeks), and multiple data types (e.g., voltage, current,  $dQ/dV$  ), limiting their practical deployment. However, to date, no framework exists that can directly map partial EIS spectra to aging-sensitive parameters with both physical interpretability and real-time performance. These trade-offs are summarized in Table 1, which compares representative methods in terms of input requirements, interpretability, and inference time, highlighting the need for a faster, more interpretable EIS-only framework.

To overcome these issues, we propose a novel framework that integrates the physical interpretability of the P2D model, the computational efficiency of Transformer-based neural networks, and a frequency-domain sensitivity structure. Rather than estimating all parameters at once, we segment the EIS spectrum into three canonical bands—low (0.01–0.63 Hz), mid (0.63–6.3 Hz), and high (6.3–100 Hz)—based on Nyquist features.

We then implement a two-stage Sobol filtering process to identify the most informative parameters across bands. First, the top three sensitive parameters are selected from one frequency band via Sobol analysis and removed from the candidate pool. A second frequency band is then analyzed to identify three more parameters from the remaining set. This results in six non-overlapping parameters tailored to specific bands, which are used to train compact, dedicated Transformer regression models

Each frequency band is paired with its own dedicated Transformer model, trained to predict three highly sensitive parameters from the real and imaginary parts of partial EIS spectra. These predicted parameters, when combined with the remaining 13 nominal values in the P2D model, are sufficient to

reconstruct the full impedance curve. The resulting reconstruction closely matches the experimental spectra (error <3%), validating both the physical consistency and predictive accuracy of the framework.

The reconstructed curves closely match the experimental measurements, with less than 3% error, validating both the physical consistency and predictive accuracy of the proposed framework. Notably, the method exhibits strong robustness: accurate inference is achieved with any two-band combination, without requiring full current–voltage history. Inference time is reduced to approximately 0.3 seconds per spectrum, making the approach suitable for real-time, embedded battery diagnostics.

The main contributions of this study can be summarized as follows:

- (1) EIS-only parameter prediction: The proposed model enables direct inference of electrochemical parameters from partial EIS spectra without relying on voltage or current histories.
- (2) Trend discovery between aging and electrochemical parameters: The predicted parameters exhibit consistent monotonic trends with decreasing SOH, capturing physically meaningful degradation behavior.
- (3) Fast, interpretable estimation: Inference time is reduced by more than two orders of magnitude—from hours (via GA) to sub-seconds—enabling, for the first time, real-time parameter estimation from EIS data.

Band-specific ML models are trained using synthetic data perturbed only by sensitive parameters. The final models accurately predict key battery parameters from EIS, balancing physical interpretability, prediction accuracy, and computational efficiency.

The following sections detail the proposed framework, including the design of synthetic training data, Sobol-based parameter selection, Transformer model structure, and impedance reconstruction validation.

## Table 1

Comparison of Parameter Identification Methods

Ref.	Estimated parameters	Time	SOH	Direct Model	Optimizer	Input data
[13]	$C_{s,neg}^0, C_{s,pos}^0, \varepsilon_{s,neg}, \varepsilon_{s,pos}, C_{s,pos}^{max}$	✗	✓	DFN	SOBOL + DL model	Partial voltage curve + $dQ/dV$
[14]	$D_s^p, D_s^n, k_p, k_n, R_{SEI}, \varepsilon_p, \varepsilon_n, \varepsilon_s$	✗	✗	P2D	GA + 1D CNN	V-I profile
[15]	26 related parameters	74+97 min (PSO)	✗	ROEspm	Two-step PSO	V-I profile
[16]	$R_{s,p}, R_{s,n}, \varepsilon_{s,p}, \varepsilon_{s,n}, \varepsilon_{e,p}, \varepsilon_{e,n}, c_{s,n}^{0\%}, c_{s,p}^{100\%}$	~ minutes	✗	SPME	EET+ PSO	V-I profile
[17]	$D_{s,p}, D_{s,n}, K_p, K_n$	✗	✗	Reduced DFN	PSO	V-I profile
[18]	25 related parameters	✗	✗	FOM	GA-PSO	EIS + DST test V & I
[19]	$L_n, L_p, R_n, k_n, R_{SEI}, c_2$	~3 weeks	✗	DFN	GA+ Fisher	V-I profile
[20]	$C_{s,neg}^0, C_{s,pos}^0, c_{0,l}, C_{s,pos}^{max}, C_{s,neg}^{max}, \varepsilon_{s,pos}, \varepsilon_{s,neg}, D_{pos}, D_{neg}, r_{s,pos}, r_{s,neg}, K_{s,pos}, K_{s,neg}$	15.2 hr + 4.7 s	✓	DFN	GA+DNN	V & I & Q & $dQ/dV$ profile
proposed	Top-3 per freq. *2 (order-dependent)	10.9hr / 0.3 s	✓	DFN	GA+SOBOL+ CNN	EIS data ( 100 Hz – 0.01 Hz )

## 2. Experimental and Modeling Workflow

Figure 1 illustrates the full experimental and modeling pipeline developed in this work. Starting from raw experimental EIS measurements on LGM50 cells, we use a physics-based P2D model and a Genetic Algorithm to obtain nominal electrochemical parameters. These serve as a foundation for Sobol sensitivity analysis, which segments the impedance spectrum into low, mid, and high frequency bands to identify key parameters. Compact ML models are then trained to estimate these sensitive parameters, enabling real-time prediction from partial EIS spectra. The following subsections detail each component of the pipeline.

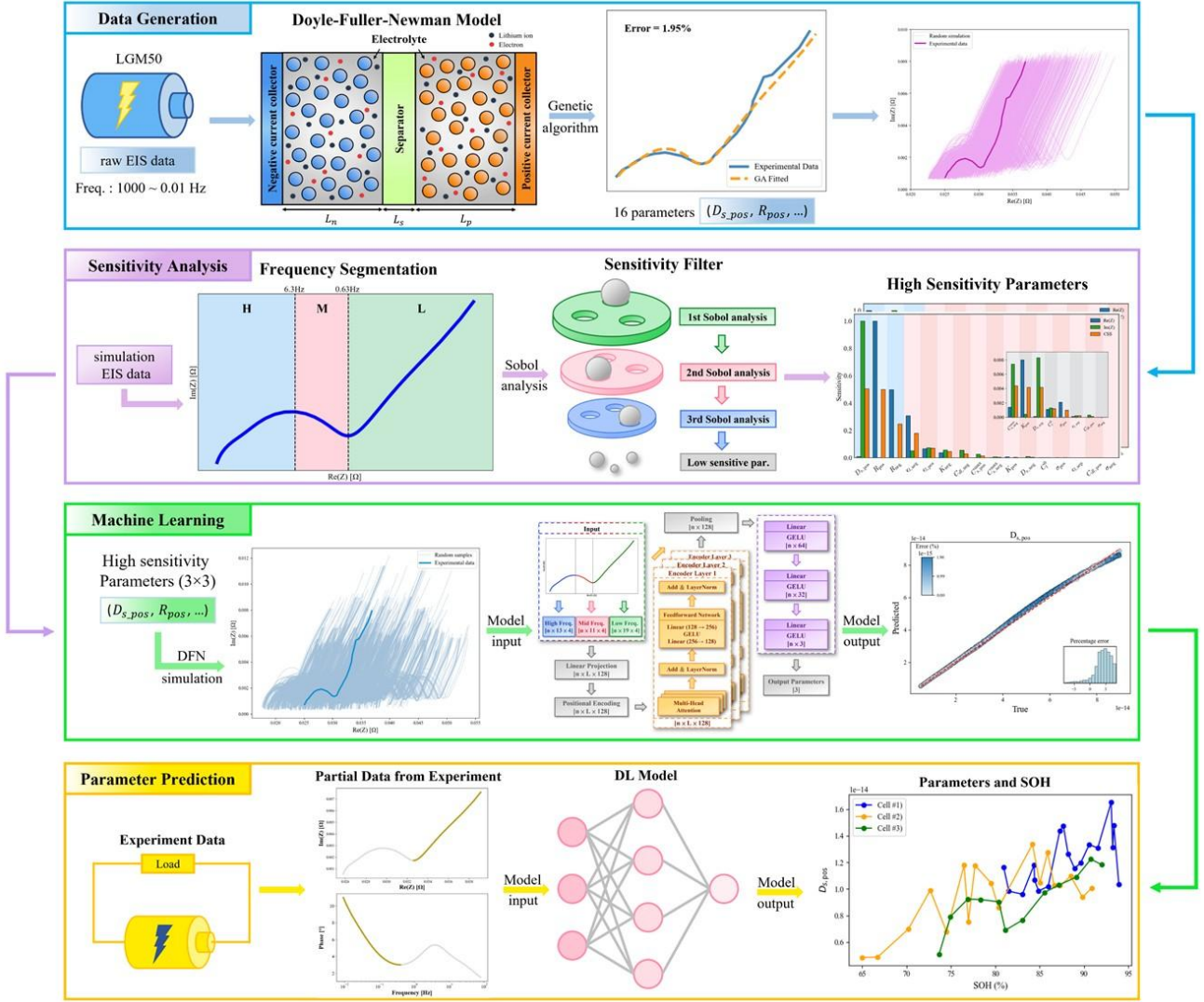


Fig 1. Overview of the experimental and modeling workflow.

## 2.1 EIS Experiment and Data Preprocessing

To obtain high-quality EIS data for inverse modeling and sensitivity analysis, diagnostic tests were conducted on three commercial LGM50LT lithium-ion cells after every 20 cycles of 1 C charge/discharge. All measurements were performed at a controlled temperature of 25 °C to ensure data consistency and reproducibility. In each diagnostic stage, cells were charged at 0.5 C to full state-of-charge and rested for 30 minutes for voltage equilibration. Without altering the state of charge, impedance spectroscopy was performed at 0.05 C over a frequency sweep from 1000 Hz down to 0.01

Hz, collecting 10 logarithmically spaced points per decade and recording both the real ( $\text{Re}(Z)$ ) and imaginary ( $\text{Im}(Z)$ ) components. Immediately following the EIS measurement, cells were discharged at 0.2 C to cutoff voltage to complete the diagnostic cycle and compute the SOH.

Among all diagnostic cycles, one EIS dataset at  $\text{SOH} = 85.54\%$  was randomly selected as the benchmark for inverse modeling and imported into COMSOL and MATLAB for subsequent fitting. Since the imaginary component of impedance was negative across the 1000 Hz to 100 Hz frequency range, all data points in this interval were removed during post-processing to focus the analysis on the physically relevant spectrum. The raw  $\text{Re}(Z)$  and  $\text{Im}(Z)$  data were used directly—without additional denoising or interpolation—for Genetic Algorithm-based parameter identification and Sobol sensitivity analysis.

## *2.2 Physics-Informed Parameter Identification using Genetic Algorithm*

The pseudo-two-dimensional (P2D) model used in this study was implemented in COMSOL Multiphysics, adapted from the experimentally validated framework in [8], to ensure high fidelity and physical consistency in EIS simulations.

To begin, we defined preliminary upper and lower bounds for all 16 electrochemical parameters based on the P2D model ranges reported in [13], while ensuring numerical stability within COMSOL. This setup ensures that all parameter combinations remain physically plausible and computationally feasible during the GA search. We then implemented a lightweight Genetic Algorithm (GA) in MATLAB, integrated with the COMSOL-based P2D model. The GA objective was to minimize a weighted Mean Relative Error (MRE) between simulated and experimental impedance data, defined as:

$$MRE_{weighted} = w_{Re} \cdot \frac{|Z_{sim,Re} - Z_{exp,Re}|}{|Z_{exp,Re}| + \varepsilon} + w_{Im} \cdot \frac{|Z_{sim,Im} - Z_{exp,Im}|}{|Z_{exp,Im}| + \varepsilon}$$

For GA hyperparameters, we used a population size of 200 and up to 50 generations, with early stopping when the global MRE fell below 2%. Each run required approximately 30 000–40 000 seconds of computation. The optimal parameter set achieved an MRE of 1.95% when fitting the SOH = 85.54% EIS benchmark spectrum. This solution was designated as the nominal parameter set and serves as the center point for subsequent range tuning and sensitivity analysis.

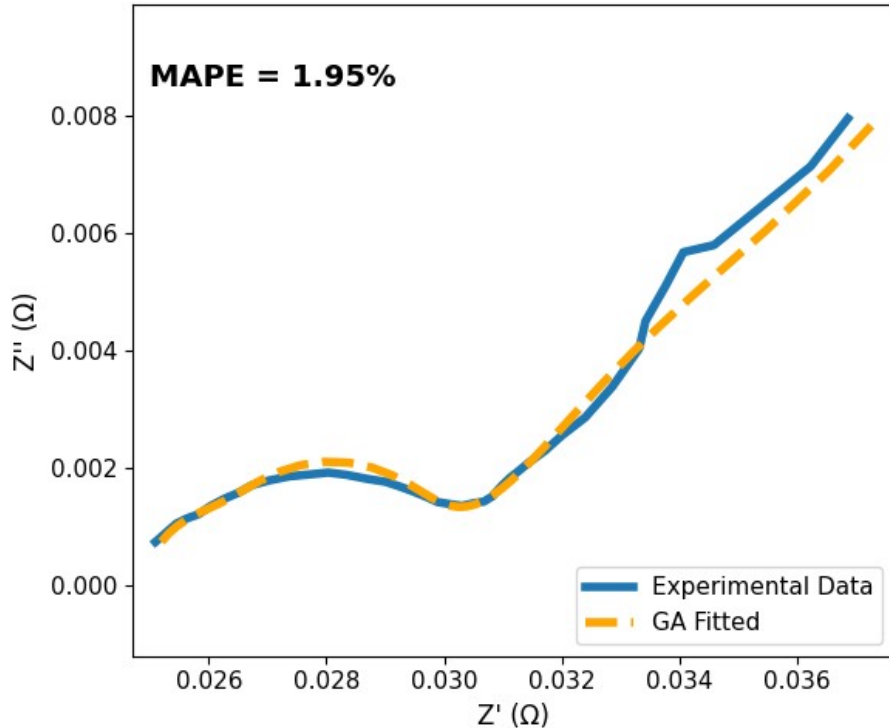


Fig 2. Comparison between experimental impedance spectrum (Cell #2, SOH  $\approx$  85%) and the P2D model fitted via genetic algorithm. The fitted result serves as the nominal parameter set for subsequent analysis.

### *2.3 Semi-Empirical Range Tuning and Sobol Sampling*

In Section 2.2, we established nominal values for the 16 electrochemical parameters by fitting the SOH = 85.54% EIS spectrum using our custom GA implementation, based on initial bounds from. For subsequent sensitivity analysis and dataset generation, we refined these bounds to ensure physical plausibility while covering the observed experimental variability. This section details our semi-

empirical tuning strategy and sampling procedure.

Starting from the nominal values obtained in Section 2.2, we applied semi-empirical adjustments to the literature-based initial bounds:

1. Generate a large set of parameter combinations and simulate their impedance responses with the COMSOL P2D model;
2. Verify that the real and imaginary components of the simulated spectra span 0.8–2× of the experimental EIS data;
3. Iteratively expand or contract any parameter bound that fails to meet the coverage criterion;

Repeat this process until all parameter bounds satisfy the 0.8–2× coverage requirement.

After tuning, we generated parameter samples using the Sobol quasi-Monte Carlo approach according to the formula:

$$N_{samples} = (d + 2) \times N$$

where d=16 is the number of parameters and N=100 is the base sample size. A total of 1800 samples were produced to explore the tuned parameter space comprehensively.

The following tables summarize the nominal values and the final adjusted bounds for all 16 electrochemical parameters:

Table 2 Geometric parameters of the electrochemical model

Symbol	Unit	Nominal	Range	References
$\varepsilon_{s,pos}$	—	0.413	0.25 – 0.55	—
$\varepsilon_{s,neg}$	—	0.666	0.45 – 0.75	—
$\varepsilon_{e,sep}$	—	0.440	0.35 – 0.65	—

Table 3 Transport parameters of the electrochemical model

Symbol	Unit	Nominal	Range	References
$D_{s,pos}$	$m^2 \cdot S^{-1}$	$9.954 \times 10^{-15}$	$5 \times 10^{-15} – 9 \times 10^{-14}$	—

$D_{s,neg}$	$m^2 \cdot S^{-1}$	$7.845 \times 10^{-14}$	$5 \times 10^{-14} - 1 \times 10^{-13}$	—
$K_{pos}$	$S \cdot m^{-1}$	10.77	0.8 – 12.0	—
$K_{neg}$	$S \cdot m^{-1}$	159.10	90 – 310	—

Table 4 Kinetic and concentration parameters of the electrochemical model

Symbol	Unit	Nominal	Range	References
$K_{r,pos}$	$m \cdot s^{-1}$	$1.5 \times 10^{-9}$	$9 \times 10^{-10} - 2.9 \times 10^{-9}$	—
$K_{r,neg}$	$m \cdot s^{-1}$	$3.3 \times 10^{-9}$	$1.8 \times 10^{-9} - 4.8 \times 10^{-9}$	—
$C_{dl,pos}$	$F \cdot m^2$	0.576	0.1 – 2	—
$C_{dl,neg}$	$F \cdot m^2$	3.380	0.01 – 10	—
$R_{pos}$	$m^2 \cdot S^{-1}$	0.042	0.01 – 0.1	—
$R_{neg}$	$m^2 \cdot S^{-1}$	0.026	0.01 – 0.05	—
$c_{s,pos}^{max}$	$mol \cdot m^{-3}$	59624	50000 – 63000	—
$c_{s,neg}^{max}$	$mol \cdot m^{-3}$	31242	27000 – 33000	—
$c_l^0$	$mol \cdot m^{-3}$	1119	1100 – 1200	—

With the bounds tuned and 1800 samples generated, we proceed in Section 2.4 to perform frequency band segmentation and Sobol sensitivity analysis to select the most influential parameter subset.

#### 2.4 Frequency Band Segmentation and Sobol Sensitivity Analysis

To identify the most influential parameters among 16 variables for different frequency ranges, we applied Sobol global sensitivity analysis in a two-stage filtering scheme on 1800 samples. Based on inflection points in the Nyquist plot, the spectrum was divided into three bands (Figure 3): H-band (100 Hz–6.3 Hz), M-band (6.3 Hz–0.63 Hz), and L-band (0.63 Hz–0.01 Hz).

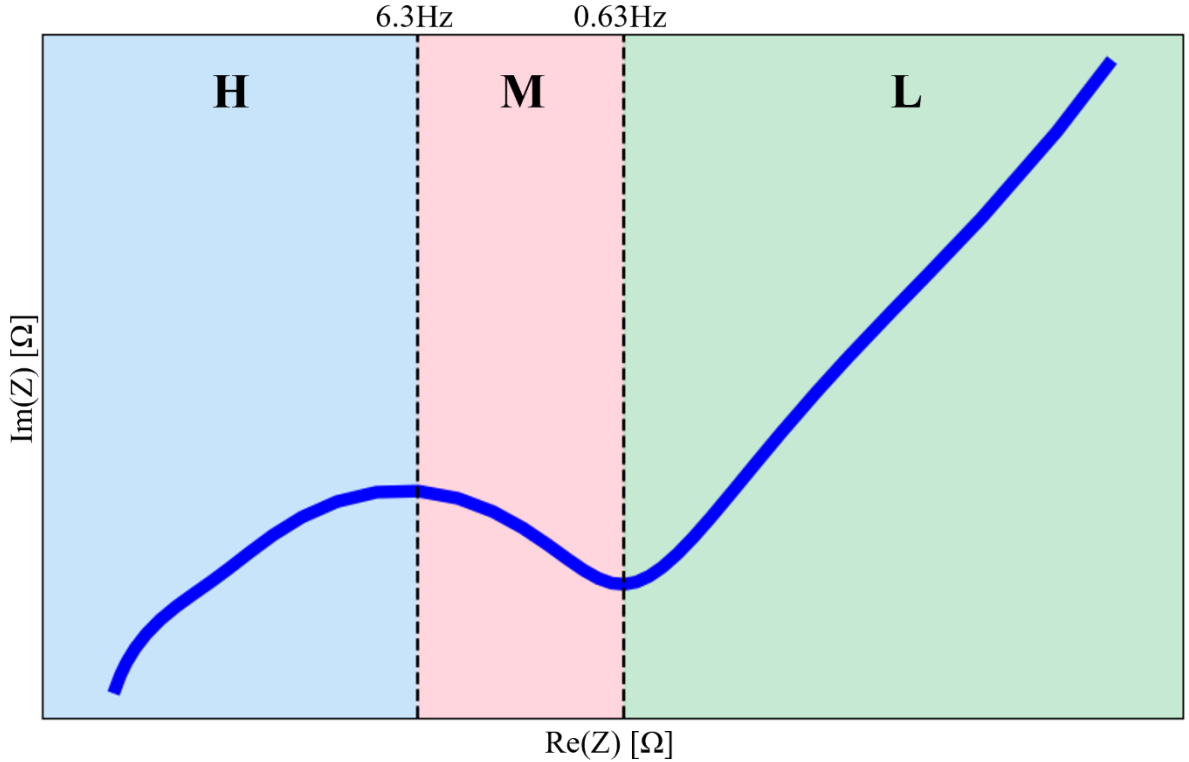


**Fig. 3.** Conceptual segmentation of Nyquist impedance into three frequency bands: H (high), M (mid), and L (low). The boundary is based on arc inflection points.

To equally weight the contributions from the real and imaginary parts, we define the Composite Sensitivity Score (CSS) as:

$$CSS = \frac{S_{Re} + S_{Im}}{2}$$

This ensures balanced weighting between the two components during parameter filtering.

Although the order of band selection does not affect the outcome, we illustrate “low-frequency first, then mid-frequency”:

1. **L-band Filtering:** Compute CSS for all 1800 samples in the L-band. Figure 4a shows  $D_{s, pos}, R_{pos}, R_{neg}$  as the top three sensitive parameters. Those in the red box have near-zero CSS and are carried forward.
2. **M-band Filtering:** Remove the three L-band parameters and compute CSS over the M-band

for the remaining 13 parameters. Figure 4b shows  $\epsilon_{l,neg}$ ,  $k_{neg}$ ,  $C_{dl,neg}$  as the top three; the red-boxed parameters again exhibit negligible sensitivity.

The six selected parameters serve as targets for Transformer regression. By feeding the predicted values along with the remaining 13 nominal parameters into the COMSOL P2D model, we reconstructed full-spectrum impedance curves with less than 2% error, validating our approach.

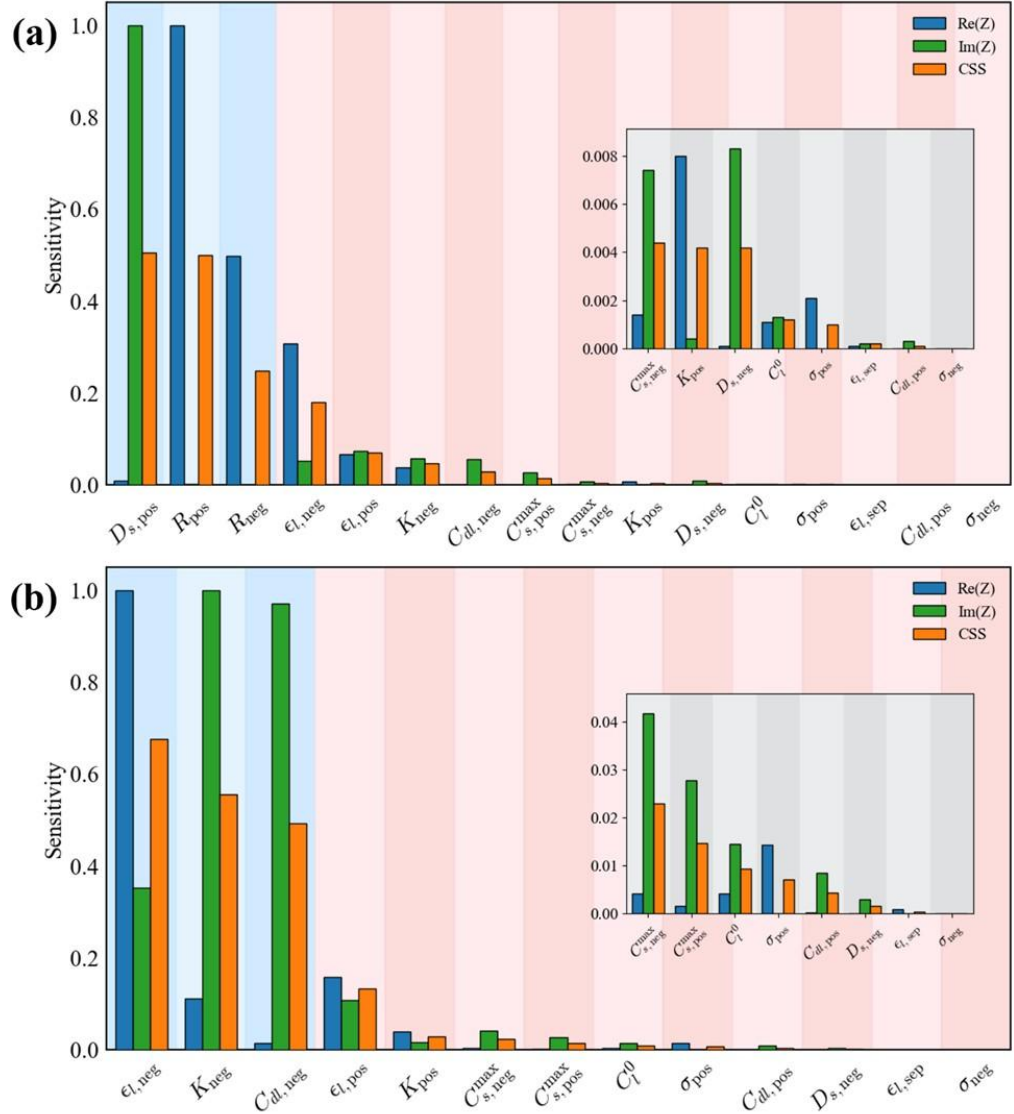


**Fig. 4.** Sobol sensitivity results. (a) Sobol sensitivity results in low-frequency band (stage 1, 16 parameters). (b) Sobol sensitivity results in mid-frequency band (stage 2, 13 remaining parameters).

Building on the tuned parameter bounds from Section 2.3, we uniformly sampled the three

sensitive parameters for each band—keeping the remaining 13 parameters at their nominal values—to produce 20,000 parameter combinations. Each combination was run through the COMSOL P2D model to simulate full EIS spectra ( $\text{Re}(Z)$  and  $\text{Im}(Z)$ ). With dataset construction complete, Chapter 3 describes frequency alignment, data preprocessing, and training of the Transformer regression models.

### 3 Transformer-Based Regression Model

#### 3.1 Input Representation & Embedding

Each input EIS segment consists of  $N$  frequency points, where  $N$  varies by band:  $N_L = 19$ ;  $N_M = 9$ ;  $N_H = 13$ . At each frequency, we construct a 4-dimensional feature vector comprising the real part  $\text{Re}(Z)$ , imaginary part  $\text{Im}(Z)$ , magnitude  $|Z|$ , and phase  $\phi$ , to fully capture both resistive and reactive characteristics of the battery impedance.

We normalize the four-dimensional features at each of the  $N$  frequency points via MinMax scaling into  $[0,1]$ , yielding  $[B,N,4]$  tensors. where  $B$  denotes the batch size, this normalization mitigates scale disparities across features and promotes stable training.

We then project the 4-dimensional features into a  $d_{model}$  – dimensional embedding space via a linear layer:

$$H_0 = \text{Linear}_{4 \rightarrow d_{model}}(X)$$

producing  $H_0 \in R^{B \times N \times d_{model}}$ . This aligns the input with the Transformer’s hidden dimensionality.

We add sinusoidal positional encodings of shape  $[1 \times N \times d_{model}]$  to  $H_0$  yielding  $H_1$ :

$$H_1 = H_0 + PE_{N \times d_{model}}$$

This injection of positional information enables the model to discern the order and spacing of frequency points, which is critical for interpreting impedance spectra.

#### 3.2 Model Architecture

Our regression model is built upon an encoder-only Transformer consisting of three stacked layers. Within each layer, the sequence undergoes multi-head self-attention—eight parallel attention

mechanisms over a 128-dimensional embedding—that computes pairwise interactions among all NNN frequency points. A residual connection and layer normalization follows this, then by a position-wise feed-forward network with a hidden dimension of 256, again wrapped in residual addition and LayerNorm to ensure stable gradients and non-linear transformation.

After three such layers, the encoder’s output tensor of shape [B, N, 128] is mean-pooled over the frequency dimension to a [B, 128] vector for each sample. The regression head first applies layer normalization to this pooled vector, then passes it through two successive fully-connected transformations with GELU activations—first reducing the dimensionality to 64, then to 32—and finally projects the 32-dimensional representation to the three target parameter values. This unified design leverages self-attention to capture global spectral dependencies, employs a moderate-sized feed-forward network to model complex nonlinearity, and uses mean pooling plus a compact MLP to map the learned representations to precise parameter estimates.

### *3.3 Training Configuration*

We optimized our Transformer regression model by minimizing the mean squared error (MSE) between the predicted and true parameter vectors. Specifically, training was driven by the AdamW optimizer with an initial learning rate set to  $1 \times 10^{-4}$  alongside a weight decay of  $1 \times 10^{-2}$  to regularize model weights. To maintain stable learning dynamics, we employed a ReduceLROnPlateau scheduler: whenever the validation loss failed to improve for ten consecutive epochs, the learning rate was halved. Additionally, gradient norms were clipped to a maximum of 1.0 to prevent exploding gradients. To guard against overfitting, we monitored validation performance and applied early stopping—terminating training if no improvement was observed over fifty epochs, with an absolute cap of 300 epochs.

We repeated this entire training procedure five times using different random seeds to assess the

robustness of our approach. After each run, the model state yielding the lowest validation loss was recorded, and upon completion, all runs were ranked—the top three models were retained for downstream evaluation and potential ensemble experiments.

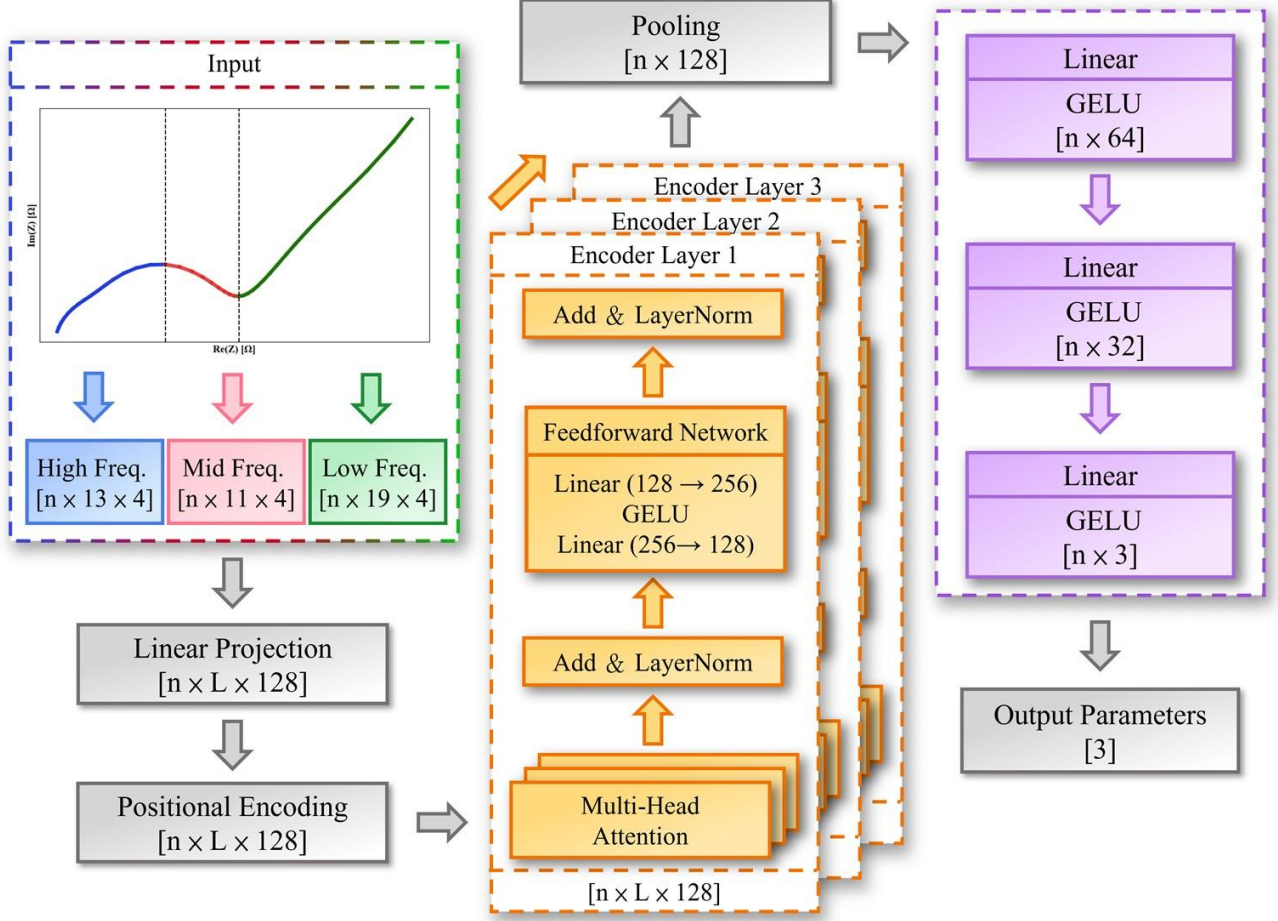


Fig. 5. Detailed structure of the Transformer model, used to output three electrochemical parameters per band.

Finally, Training and evaluation were performed on a workstation equipped with an Intel Core™ i5-14600K CPU clocked at 3.5 GHz (up to 5.6 GHz Turbo), 32 GB of DDR5 RAM, and integrated Intel® UHD Graphics 770.

#### 4. Result and Discussion

#### 4.1. Model Performance Comparison

To quantitatively compare the predictive accuracy of our three architectures—CNN, Transformer, and BiLSTM—we evaluate each on the low-frequency test set and report the distribution of mean relative error (MRE) across all samples. Figure 6 presents bar plots of the average MRE with error bars indicating  $\pm 1$  standard deviation and the full min–max range. Table 5 summarizes key statistics: mean, standard deviation, minimum and maximum MRE, as well as average training and inference times.

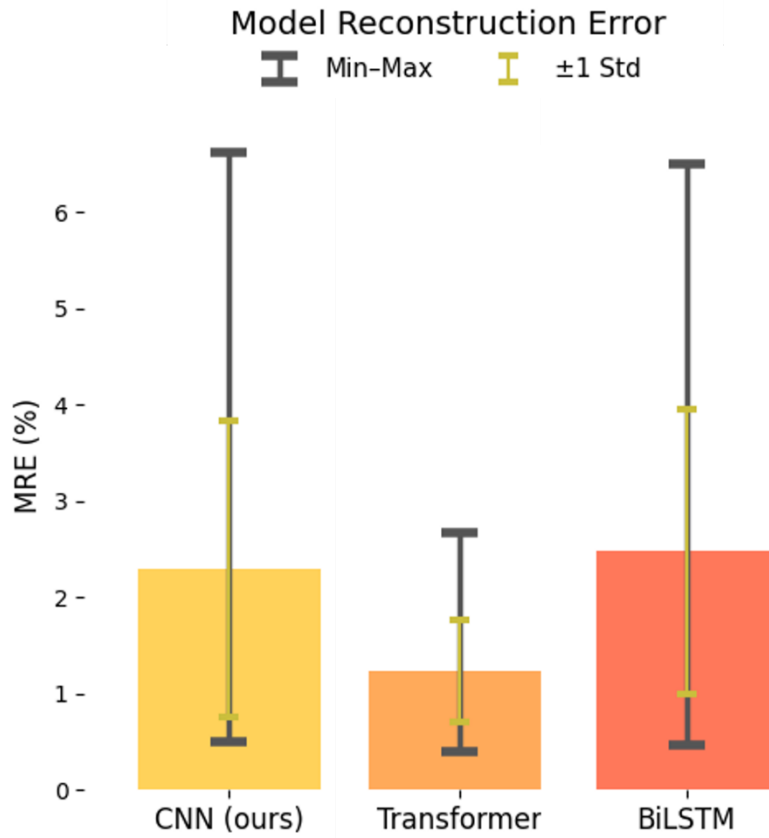


**Fig. 6.** Comparison of low-frequency impedance reconstruction error for CNN, Transformer, and BiLSTM models

**Table 5** low-frequency impedance reconstruction errors and computational costs.

Model	Mean MRE(%)	Std(%)	Min MRE(%)	Max MRE(%)	Avg predict time(s)
CNN	2.30	1.54	0.50	6.62	0.6
<b>Transformer</b>	<b>1.24</b>	<b>0.53</b>	<b>0.39</b>	<b>2.68</b>	<b>0.3</b>
BiLSTM	2.48	1.48	0.46	6.50	0.7

From both the bar plots and summary table, the Transformer model consistently outperforms CNN and BiLSTM in accuracy, achieving the lowest mean MRE (1.24 %), the tightest error distribution ( $\sigma = 0.53 \%$ ), and the smallest maximum error (2.68 %).

The Transformer’s superior performance can be attributed to its self-attention mechanism, which captures long-range dependencies across all N frequency points and enables more precise inference of the three sensitive parameters from partial spectra. In contrast, the CNN’s local receptive fields may miss non-local interactions, and the BiLSTM—though modeling sequential dependencies—suffers from vanishing gradients over long sequences and higher computational overhead.

In terms of computational efficiency, while the Transformer demands the longest training time due to its attention complexity, training duration is a one-time cost—what truly matters for deployment is inference latency. The Transformer achieves the fastest prediction speed (0.3 s per sample), making it ideally suited for real-time or near-real-time parameter estimation. By comparison, the CNN model trains quickly but has slower inference, and the BiLSTM falls in between.

Overall, these results underscore that inference speed, rather than training time, is the critical factor for practical applications: the Transformer delivers the lowest errors with the responsiveness

required for timely battery health monitoring.

#### *4.2 Parameter Trends with State-of-Health*

To visualize how our Transformer model captures aging dynamics, we fed the experimental low-frequency EIS spectra from three individual cells into the trained low-frequency Transformer and obtained predicted values for the three sensitive parameters at each SOH measurement. Connecting these points in ascending SOH order yields the trend curves shown in Figure 7 To visualize how our Transformer model captures aging dynamics, we fed the experimental low-frequency EIS spectra from three individual cells into the trained low-frequency Transformer and obtained predicted values for the three sensitive parameters at each SOH measurement. Connecting these points in ascending SOH order yields the trend curves shown in Figure 7.

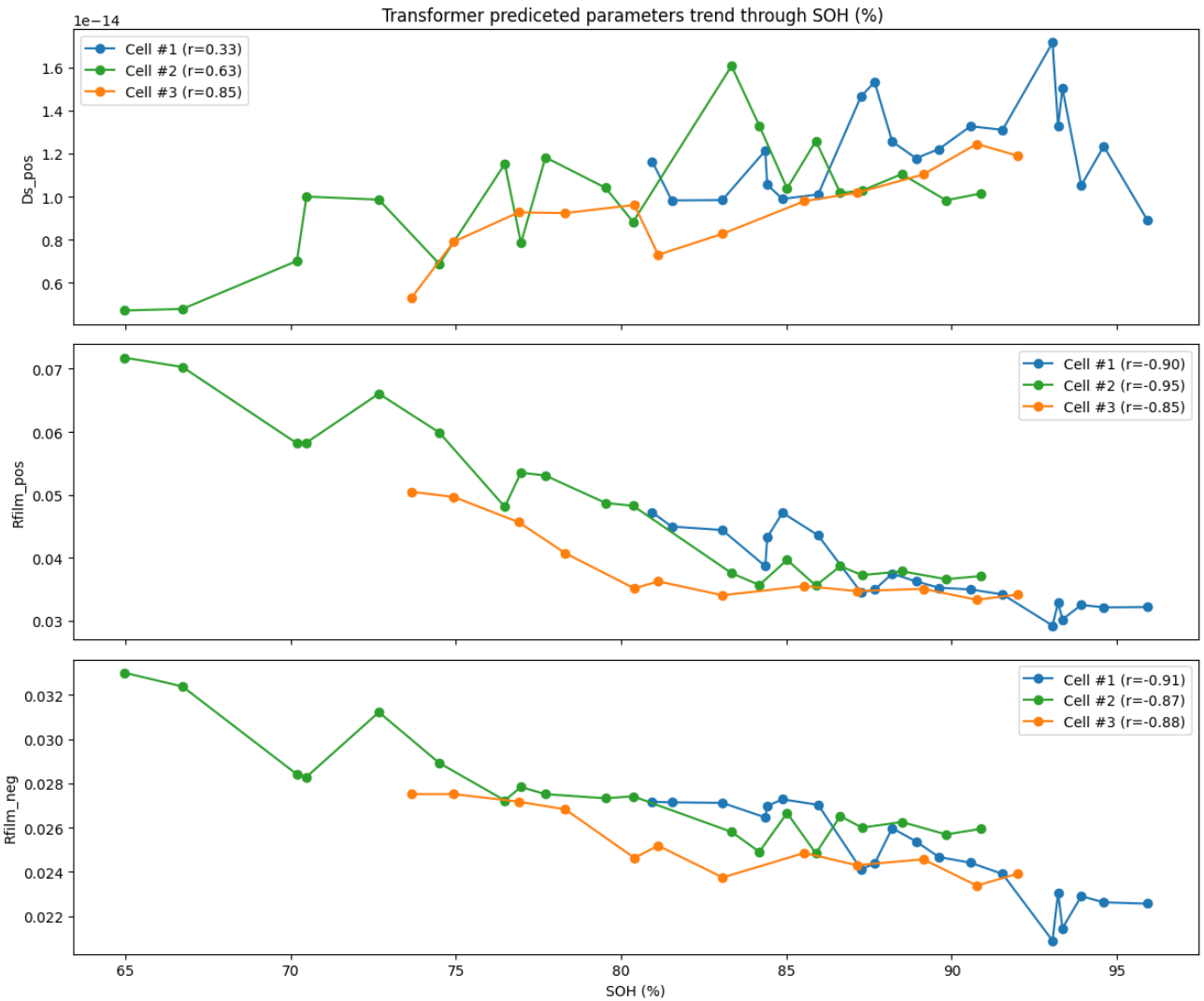


**Fig. 7.** Transformer-predicted parameter trends versus SOH for Cells #1–#3. Markers indicate individual EIS tests; lines connect measurements in increasing SOH order.

We quantify the strength of these trends via Pearson’s correlation coefficient  $r$  between SOH and each predicted parameter (Table 6).

**Table 6** Pearson correlation coefficients between SOH and Transformer-predicted parameters.

Parameters	Cell#1 r	Cell#2 r	Cell#3 r	Avg r

$D_{s,pos}$	0.330	0.627	0.849	0.602
$R_{film,pos}$	-0.902	-0.952	-0.848	-0.901
$R_{film,neg}$	-0.907	-0.873	-0.883	-0.888

From Figure 7 and Table 6, the model faithfully reproduces known aging behaviors:

- Solid-phase diffusion coefficient  $D_{s,pos}$  decreases as SOH declines (average  $r=0.602$ ), in line with diminished lithium mobility due to electrode degradation [26–28].
- Film resistance  $R_{film,pos}$  and  $R_{film,neg}$  increase strongly with aging (average  $r \approx -0.90$ ), reflecting SEI/interface thickening and growing impedance, as observed in EIS studies of aged cells [29].

This agreement with experimental literature confirms that our Transformer not only minimizes reconstruction error but also captures the underlying electrochemical aging mechanisms, thereby providing interpretable parameter estimates for battery health monitoring.

#### 4.3 Segment-Spectrum Reconstruction Examples

To demonstrate the Transformer model’s ability to reconstruct the low-frequency (0.63–0.01 Hz) impedance arc across the SOH spectrum, we selected four representative cases spanning from high to low health states. Figure 8 overlays the experimental Nyquist segment (green dashed line) with the Transformer reconstructions (orange solid line), and annotates the MAPE, RMSE, and MAE for each subplot:

### Low freq. Nyquist comparison: Exp vs Transformer

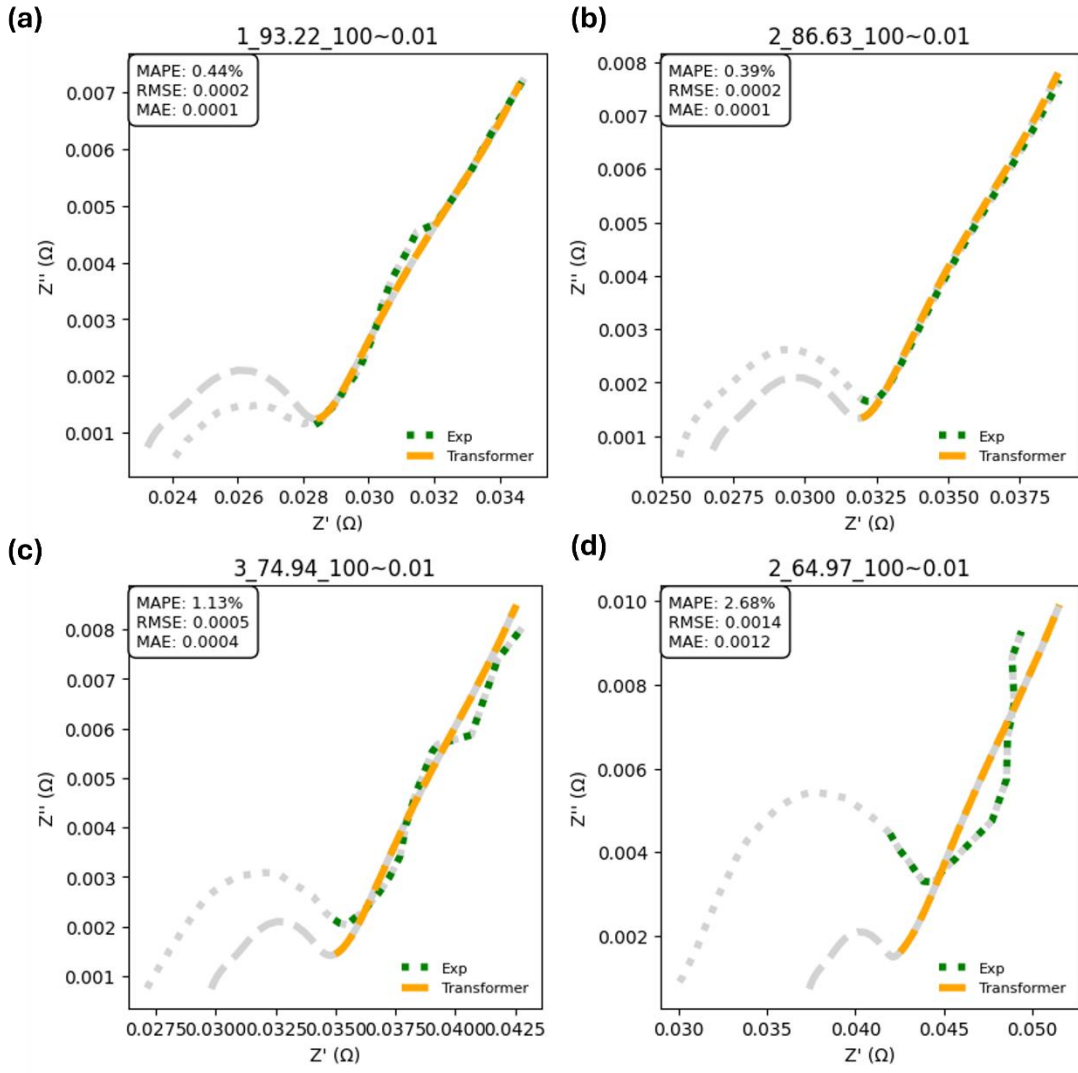


**Fig. 8.** Low-frequency Nyquist segment reconstruction (Transformer) (a) SOH = 93.22 %, MAPE = 0.44 % ; (b) SOH = 86.63 %, MAPE = 0.39 % ; (c) SOH = 74.94 %, MAPE = 1.13 % ; (d) SOH = 64.97 %, MAPE = 2.68 %

In cases (a) and (b), with SOH above 85 %, the model achieves exceptional low-frequency fits (MAPE < 0.5 %) and the reconstructed arc nearly coincides with the experimental data. At SOH of 74.94 % (c), the error rises to 1.13 %, yet the overall trend remains well captured. Under severe aging at SOH = 64.97 % (d), the low-frequency arc exhibits pronounced distortion and noise, pushing MAPE to 2.68 % and causing visible deviations.

These results confirm that for  $\text{SOH} \geq 75\%$ , our Transformer–P2D pipeline delivers high-accuracy low-frequency reconstructions ( $\text{MAPE} < 1.2\%$ ), validating its suitability for online health monitoring in early to mid-life battery conditions. At very low SOH, reconstruction quality decreases, suggesting that future enhancements—such as low-SOH data augmentation or partial mid-frequency inputs—could further improve performance in advanced aging scenarios.

#### 4.4 Reconstruction Error versus SOH

Figure 9 plots the mean absolute percentage error (MAPE) of the Transformer’s low-frequency (0.63–0.01 Hz) Nyquist arc reconstructions against battery state of health (SOH). Each marker corresponds to one EIS measurement, and the connecting line reveals the trend from  $\text{SOH} \approx 95\%$  down to  $\approx 65\%$ . At high health states ( $\text{SOH} \geq 85\%$ ), reconstruction errors remain very low—typically 0.4%–1.0%, with many points under 0.5%—demonstrating the model’s robustness in early life.

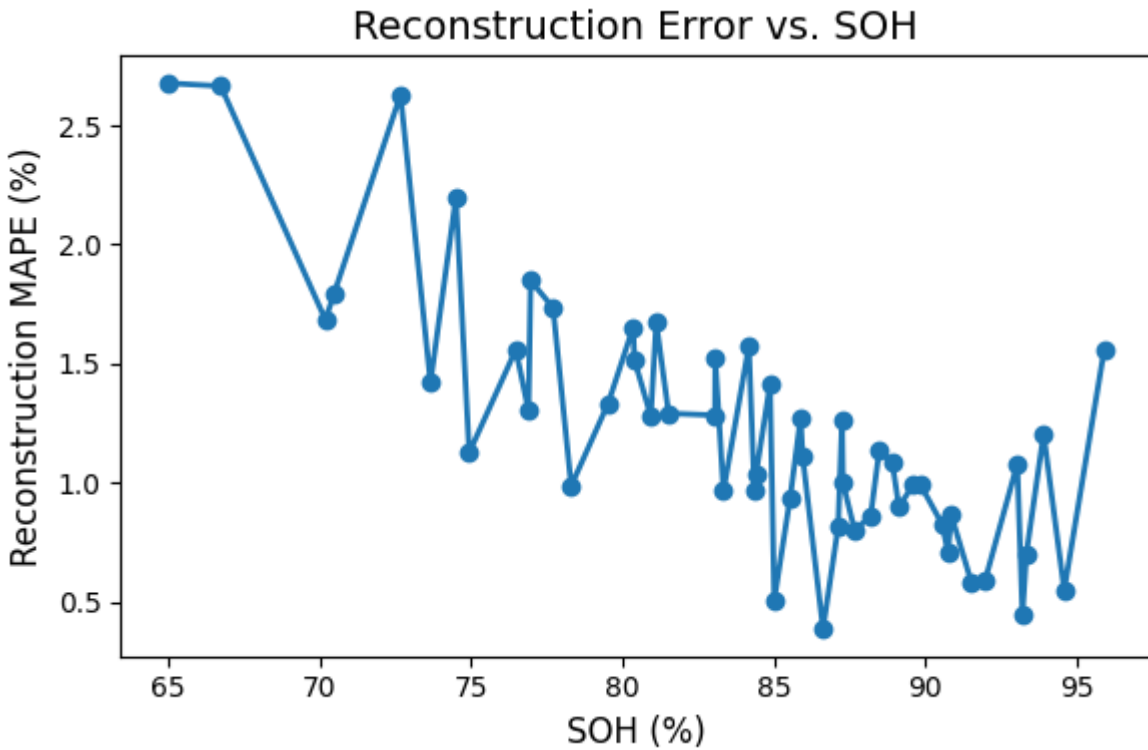


**Fig. 9.** Low-frequency reconstruction error (MAPE) versus SOH for Transformer predictions

As SOH declines into mid-range (75 %–85 %), MAPE gradually increases to 1.0 %–2.0 %, reflecting subtle changes in the low-frequency arc shape. Under severe aging (SOH  $\leq$  75 %), the experimental Nyquist curves often exhibit additional scatter or slight offset—due largely to instrumentation noise and cell-to-cell variability—causing MAPE to exceed 2 % and display greater dispersion. Importantly, even in these cases, the Transformer’s reconstructed arc faithfully follows the overall trend of the experimental data, indicating that most of the apparent “distortion” arises from measurement artifacts rather than a fundamental model failure.

Critically, for SOH  $\geq$  80 %, the Transformer–P2D pipeline maintains MAPE below 1.5 %, satisfying accuracy requirements for online health monitoring and early-warning diagnostics. The predictable rise in error at low SOH suggests clear paths for future improvement—such as augmenting training data with more low-SOH measurements or selectively incorporating mid-frequency features—to extend high-fidelity reconstruction into advanced aging regimes.

#### *4.5 Performance Across Frequency Bands*

Figure 9 displays four representative mid-frequency (6.3–0.63 Hz) Nyquist arcs reconstructed by our Transformer model—each subplot overlays the experimental segment (green dashed line) with the Transformer output (orange solid line), and reports MAPE, RMSE, and MAE. As the battery degrades from SOH  $\approx$  92 % down to  $\approx$  67 %, the mid-frequency reconstruction error grows in a predictable fashion.

### Mid freq. Nyquist comparison: Exp vs Transformer

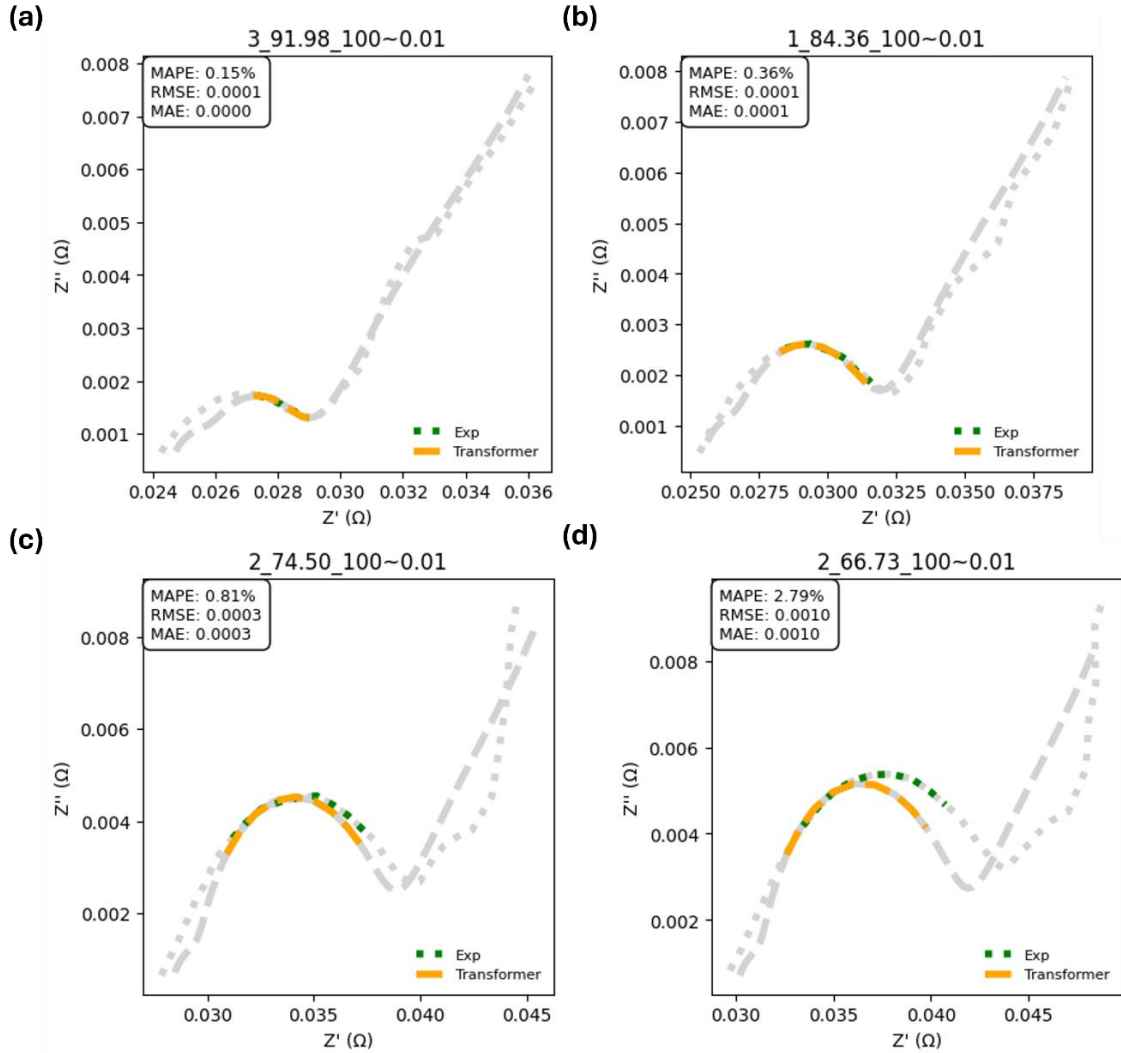


Fig. 9. Mid-frequency Nyquist segment reconstruction (a) SOH = 91.98 %, MAPE = 0.15 % ; (b) SOH = 84.36 %, MAPE = 0.36 % ; (c) SOH = 74.50 %, MAPE = 0.81 % ; (d) SOH = 66.73 %, MAPE = 2.79 %

In the nearly fresh cell (SOH = 91.98 %), the model attains an impressively low MAPE of 0.15 %, demonstrating that even the less-sensitive mid-frequency band can yield highly accurate parameter inference. As SOH falls to 84.36 %, MAPE increases gently to 0.36 %, and remains below 1 % until the battery enters moderate aging (SOH = 74.50 %, MAPE = 0.81 %). Only under severe degradation (SOH = 66.73 %) does MAPE approach 2.8 %, reflecting the intrinsic challenge of capturing

pronounced spectral shifts amid aging-induced noise.

Crucially, these results reaffirm our central premise: each frequency segment—low or mid—can independently support rapid, accurate parameter prediction and impedance reconstruction, without requiring cross-band inputs. For the vast majority of the cell’s life ( $\text{SOH} \geq 75\%$ ), mid-frequency reconstructions maintain sub-1 % MAPE, more than adequate for real-time health monitoring. In the rare late-stage aging cases where errors rise, targeted improvements—such as augmenting the mid-frequency training set with severely aged spectra or applying noise-robust regularization—can further strengthen single-segment performance, all while preserving the simplicity and speed of our approach.

#### *4.6 Ablation Study on Segment Length and Noise*

## **5. Conclusion**

In this work, we have demonstrated a rapid and interpretable framework for electrochemical parameter estimation from partial EIS measurements. By combining physics-based GA inversion, Sobol sensitivity filtering, and segment-specific Transformer regression, our method requires only a small subset of the impedance spectrum—low, mid, or high frequency—to accurately predict key model parameters and reconstruct the corresponding Nyquist arc.

Key achievements include:

1. Efficient Nominal Parameter Identification: A Genetic Algorithm applied to a P2D model generated high-fidelity nominal parameters ( $MRE \approx 1.95\%$ ) from a single EIS reference spectrum ( $SOH \approx 85\%$ ).
2. Frequency-Resolved Sensitivity Selection: Two-stage Sobol analysis distilled 16 parameters down to the three most influential ones in each segment, enabling focused, low-dimensional regression.
3. Transformer-Based Segment Regression: Separate Transformer models trained on 20,000 simulated samples achieved sub-1 % MAPE on low- and mid-frequency segments for  $SOH \geq 75\%$ , and produced full-spectrum reconstructions with <2 % error.
4. Practical Online Applicability: Single-segment inference requires only 19 low-frequency or 9 mid-frequency points, runs in <0.5 s per sample on modest hardware, and maintains accuracy throughout the battery's early-to-mid life.

These results validate that partial-spectrum EIS, when guided by physics-informed sensitivity analysis, can serve as a fast, accurate, and resource-efficient diagnostic tool for battery health monitoring.

Future work will extend this framework to in-field datasets, explore adaptive online learning for extreme aging regimes, and investigate multi-segment fusion strategies to further enhance robustness across the entire lifetime.

## **acknowledgment**

This work was supported by the National Science and Technology Council R.O.C. under Grant NSTC 112-2221-E-002-253-MY3.

## **Reference**

- [1] C. Rabissi, A. Innocenti, G. Sordi, A. Casalegno, “A Comprehensive Physical-Based Sensitivity Analysis of the Electrochemical Impedance Response of Lithium-Ion Batteries,” *Energy Technology*, vol. 9, no. 3, 2021.
- [2] B. Wimarshana, I. Bin-Mat-Arishad, A. Fly, “A multi-step parameter identification of a physico-chemical lithium-ion battery model with electrochemical impedance data,” *Journal of Power Sources*, vol. 580, 2023, 233400.
- [3] C.-J. Ko, K.-C. Chen, “Constructing battery impedance spectroscopy using partial current in constant-voltage charging or partial relaxation voltage,” *Applied Energy*, vol. 356, 2024, 122454. <https://doi.org/10.1016/j.apenergy.2023.122454>
- [4] C. Chang, L. Chen, X. Liu, et al., “Electrochemical aging model of lithium-ion battery with impedance output and its parameter sensitivity analysis and identification,” *Journal of Energy Storage*, vol. 86, 2024, 111277. <https://doi.org/10.1016/j.est.2024.111277>
- [5] B.-C. Wang, Y.-B. He, J. Liu, B. Luo, “Fast parameter identification of lithium-ion batteries via classification model-assisted Bayesian optimization,” *Energy*, vol. 288, 2024, 129667. <https://doi.org/10.1016/j.energy.2023.129667>
- [6] H. Nunes, J. Martinho, J. Fermeiro, J. Pombo, S. Mariano, and M. R. Calado, “Impedance Analysis and Parameter Estimation of Lithium-Ion Batteries Using the EIS Technique,” *IEEE Transactions on Industry Applications*, vol. 60, no. 3, pp. 5048–5060, 2024. <https://doi.org/10.1109/TIA.2024.3365451>
- [7] X. Duan, F. Liu, E. Agar, and X. Jin, “Parameter Identification of Lithium-Ion Batteries by Coupling Electrochemical Impedance Spectroscopy with a Physics-Based Model,” *Journal of The Electrochemical Society*, vol. 169, no. 4, 2022, 040561. <https://doi.org/10.1149/1945-7111/ac682f>
- [8] B. Wimarshana, I. Bin-Mat-Arishad, A. Fly, “Parameter sensitivity analysis of a physico-chemical lithium-ion battery model with combined discharge voltage and electrochemical impedance data,” *Journal of Power Sources*, vol. 527, 2022, 231125. <https://doi.org/10.1016/j.jpowsour.2022.231125>
- [9] W. Li, D. Cao, D. Jöst, et al., “Parameter sensitivity analysis of electrochemical model-based battery management systems for lithium-ion batteries,” *Applied Energy*, vol. 269, 2020, 115104. <https://doi.org/10.1016/j.apenergy.2020.115104>
- [10] X. Shen, X. Li, S. Niu, L. Du, “Sensitivity analysis and identification of battery physicochemical model parameters under different temperature impedances,” *Journal of Energy Storage*, vol. 101, 2024, 113891. <https://doi.org/10.1016/j.est.2024.113891>

- [11] W. Tang, G. Chang, J. Xie, X. Pan, H. Yuan, J. Shen, X. Wei, H. Dai, “Enhanced understanding of electrothermal dynamics kinetic behavior for commercial-size PEM fuel cells based on impedance and distributed temperature measurement,” *International Journal of Heat and Mass Transfer*, vol. 225, 125955, 2024. <https://doi.org/10.1016/j.ijheatmasstransfer.2024.125955>
- [12] L. Zhao, H. Dai, F. Pei, P. Ming, X. Wei, J. Zhou, “A Comparative Study of Equivalent Circuit Models for Electro-Chemical Impedance Spectroscopy Analysis of Proton Exchange Membrane Fuel Cells,” *Energies*, vol. 15, no. 1, p. 386, 2022. <https://doi.org/10.3390/en15010386>
- [13] C.-J. Ko, C.-W. Lu, K.-C. Chen, C.-H. Chen, “Using partial discharge data to identify highly sensitive electrochemical parameters of aged lithium-ion batteries,” *Energy Storage Materials*, vol. 71, 2024, 103665. <https://doi.org/10.1016/j.ensm.2024.103665>
- [14] Kim, J., Chun, H., Baek, J., & Han, S. (2022). Parameter identification of lithium-ion battery pseudo-2-dimensional models using genetic algorithm and neural network cooperative optimization. *Journal of Energy Storage*, 45, 103571. <https://doi.org/10.1016/j.est.2021.103571>
- [15] G. Fan, “Systematic parameter identification of a control-oriented electrochemical battery model and its application for state of charge estimation at various operating conditions,” *Journal of Power Sources*, vol. 476, 2020, 228153. <https://doi.org/10.1016/j.jpowsour.2020.228153>
- [16] Wang, J., Meng, J., Peng, Q., Liu, T., Zeng, X., Chen, G., & Li, Y. (2023). Lithium-ion battery state-of-charge estimation using electrochemical model with sensitive parameters adjustment. *Batteries*, 9(3), 180. <https://doi.org/10.3390/batteries9030180>
- [17] M.A. Rahman, S. Anwar, A. Izadian, “Electrochemical model parameter identification of a lithium-ion battery using particle swarm optimization method,” *Journal of Power Sources*, vol. 307, 2016, pp. 86–97. <https://doi.org/10.1016/j.jpowsour.2015.12.083>
- [18] L. Zhang, X. Wang, M. Chen, F. Yu, M. Li, “A fractional-order model of lithium-ion batteries and multi-domain parameter identification method,” *Journal of Energy Storage*, vol. 50, 2022, 104595. <https://doi.org/10.1016/j.est.2022.104595>
- [19] J.C. Forman, S.J. Moura, J.L. Stein, H.K. Fathy, “Genetic identification and Fisher identifiability analysis of the Doyle–Fuller–Newman model from experimental cycling of a LiFePO<sub>4</sub> cell,” *Journal of Power Sources*, vol. 210, 2012, pp. 263–275. <https://doi.org/10.1016/j.jpowsour.2012.03.009>
- [20] W.-J. Lin, K.-C. Chen, “Evolution of parameters in the Doyle–Fuller–Newman model of cycling lithium-ion batteries by multi-objective optimization,” *Applied Energy*, vol. 314, 2022, 118925. <https://doi.org/10.1016/j.apenergy.2022.118925>
- [21] Yu-Chuan Chien, H. Liu, A. S. Menon, W. R. Brant, D. Brandell, M. J. Lacey, “Rapid determination of solid-state diffusion coefficients in Li-based batteries via intermittent current interruption method,” *Nature Communications*, vol. 14, article no. 2245, 2023. <https://doi.org/10.1038/s41467-023-37989-6>
- [22] O. Capron, R. Gopalakrishnan, N. Omar, J. Van Mierlo, J. Jaguemont, P. Van Den Bossche, “On the Ageing of High Energy Lithium-Ion Batteries—Comprehensive Electrochemical Diffusivity Studies of Harvested Nickel Manganese Cobalt Electrodes,” *Materials*, vol. 11, no. 2, 176, 2018. doi:10.3390/ma11020176
- [23] V. Charbonneau, A. Lasia, G. Brisard, “Impedance studies of Li<sup>+</sup> diffusion in nickel manganese cobalt oxide (NMC) during charge/discharge cycles,” *Journal of Electroanalytical Chemistry*, vol. 878, 113944, 2020. <https://doi.org/10.1016/j.jelechem.2020.113944>
- [24] S. Song, X. Zhang, Y. An, T. Hu, C. Sun, L. Wang, C. Li, X. Zhang, K. Wang, Z. J. Xu, X. Sun, Y. Ma, “Floating aging mechanism of lithium-ion capacitors: Impedance model and post-mortem analysis,” *Journal of Power Sources*, vol. 538, 232597, 2022. <https://doi.org/10.1016/j.jpowsour.2022.232597>
- [25] M. Schalenbach, B. Wu, C.-L. Tsai, A. Windmüller, L. Raijmakers, S. Yu, H. Tempel, R.-A. Eichel, “Double layer capacitance as a sensitive metric to monitor the formation of solid

- electrolyte interphases in Li–ion batteries,” *Energy Advances*, vol. 4, pp. 140–151, 2025.  
<https://doi.org/10.1039/D4YA00524D>
- [26] Y.-C. Chien, H. Liu, A. S. Menon, W. R. Brant, D. Brandell, M. J. Lacey, “Rapid determination of solid-state diffusion coefficients in Li-based batteries via intermittent current interruption method,” *Nature Communications*, vol. 14, Article number: 2289, 2023.  
<https://doi.org/10.1038/s41467-023-37989-6>
- [27] O. Capron, R. Gopalakrishnan, J. Jaguemont, P. Van Den Bossche, N. Omar, J. Van Mierlo, “On the Ageing of High Energy Lithium-Ion Batteries—Comprehensive Electrochemical Diffusivity Studies of Harvested Nickel Manganese Cobalt Electrodes,” *Materials*, vol. 11, 176, 2018.  
<https://doi.org/10.3390/ma11020176>
- [28] V. Charbonneau, A. Lasia, G. Brisard, “Impedance studies of Li<sup>+</sup> diffusion in nickel manganese cobalt oxide (NMC) during charge/discharge cycles,” *Journal of Electroanalytical Chemistry*, vol. 875, 113944, 2020. <https://doi.org/10.1016/j.jelechem.2020.113944>
- [29] J. Guo, S. Jin, X. Sui, X. Huang, Y. Xu, Y. Li, P. K. Kristensen, D. Wang, K. Pedersen, L. Gurevich, D.-I. Stroe, “Unravelling and quantifying the aging processes of commercial Li(Ni<sub>0.5</sub>Co<sub>0.2</sub>Mn<sub>0.3</sub>)O<sub>2</sub>/graphite lithium-ion batteries under constant current cycling,” *J. Mater. Chem. A*, vol. 11, pp. 41–52, 2023. <https://doi.org/10.1039/D2TA05960F>
- [30]